



Article

# Characterization and Optimization of Cu-Al<sub>2</sub>O<sub>3</sub> Nanocomposites Synthesized via High Energy Planetary Milling: A Morphological and Structural Study

Mohammad Rezayat <sup>1,\*</sup>, Mojtaba Karamimoghadam <sup>2</sup>, Omid Ashkani <sup>3</sup> and Mahdi Bodaghi <sup>4,\*</sup>

- <sup>1</sup> Center for Structural Integrity, Micromechanics and Reliability of Materials (CIEFMA), Department of Materials Science and Engineering, Universitat Politècnica de Catalunya—BarcelonaTECH, 08019 Barcelona, Spain
- <sup>2</sup> Department of Mechanics, Mathematics and Management, Polytechnic University of Bari, Via Orabona 4, 70125 Bari, Italy
- <sup>3</sup> Department of Materials Science and Engineering, Faculty of Engineering, Azad University, Science and Research Branch, Tehran 1477893855, Iran
- <sup>4</sup> Department of Engineering, School of Science and Technology, Nottingham Trent University, Nottingham NG11 8NS, UK
- \* Correspondence: mohammad.rezayat@upc.edu (M.R.); mahdi.bodaghi@ntu.ac.uk (M.B.)

**Abstract:** This study examines the synthesis and characterization of a copper–alumina nanocomposite powder. Mechanical milling is employed to synthesize the powder, and a holistic analysis is conducted to evaluate its morphological and structural properties. TEM analysis reveals the presence of alumina particles within the copper matrix, indicating the formation of both coarse and fine particles at different stages of synthesis. XRD analysis demonstrates a reduction in copper’s crystallite size with increasing milling time, attributed to defects generated within the crystal lattice during milling. Additionally, statistical analysis is utilized to determine the significance of different factors influencing the synthesis process. ANOVA analysis reveals that milling time has a significant impact on the particle size of the nanocomposite powder, while temperature and their interaction do not exhibit significant effects. Optimization techniques are utilized to identify solutions that meet the specified constraints for milling time, temperature, particle size, and differential thermal response, resulting in favorable solutions within the desired ranges. The study highlights the efficacy of mechanical milling for producing nanocomposite powders with enhanced mechanical properties, offering promising prospects for advanced materials in various industries. Additionally, the characterization results provide valuable insights into the microstructure and phase distribution of the nanocomposite powder. The application of the Williamson–Hall method proves to be effective in determining the crystallite size of the synthesized powder.

**Keywords:** Cu–Al<sub>2</sub>O<sub>3</sub> nanocomposites; high energy planetary milling; powder metallurgy; microstructure; mechanical properties



**Citation:** Rezayat, M.; Karamimoghadam, M.; Ashkani, O.; Bodaghi, M. Characterization and Optimization of Cu–Al<sub>2</sub>O<sub>3</sub> Nanocomposites Synthesized via High Energy Planetary Milling: A Morphological and Structural Study. *J. Compos. Sci.* **2023**, *7*, 300. <https://doi.org/10.3390/jcs7070300>

Academic Editors: Francesco Tornabene and Thanasis Triantafyllou

Received: 1 July 2023  
Revised: 13 July 2023  
Accepted: 19 July 2023  
Published: 22 July 2023



**Copyright:** © 2023 by the authors. Licensee MDPI, Basel, Switzerland. This article is an open access article distributed under the terms and conditions of the Creative Commons Attribution (CC BY) license (<https://creativecommons.org/licenses/by/4.0/>).

## 1. Introduction

The development of nanotechnology has led to significant progress in the synthesis and characterization of nanostructured materials. In particular, the production of metal matrix nanocomposites has gained significant attention due to their unique mechanical, thermal, and electrical properties. Copper-based nanocomposites have been studied extensively due to the high thermal and electrical conductivity of copper [1–4], as well as its low cost and availability [5,6]. The incorporation of ceramic nanoparticles, such as alumina, into the copper matrix can improve the mechanical properties [7,8], such as hardness and wear resistance, without compromising the electrical and thermal conductivity [9–11].

The synthesis of copper–alumina nanocomposites can be achieved through various methods, including powder metallurgy, electrodeposition, and mechanical milling [12–14].

Mechanical milling has been a widely studied method due to its effectiveness in achieving a uniform dispersion of nanoparticles in the copper matrix [15–17]. In this method, the mechanical energy generated by high-energy milling causes deformation, cold welding, and fracturing of the powder particles, resulting in the formation of nanocomposite powders [18,19]. Mechanical milling is a solid-state powder processing technique that involves the high-energy collision of milling balls or pellets with the powder particles. The mechanical energy generated during milling causes deformation, cold welding, and fracturing of the powder particles, resulting in the formation of nanocrystalline or amorphous powders [20–24]. A study by Dash et al. [25] investigated the mechanical properties of copper–alumina nanocomposites synthesized by powder metallurgy. The results show that the addition of alumina nanoparticles improved the hardness and wear resistance of the copper matrix without affecting its electrical conductivity. The authors attributed the improvement in mechanical properties to the uniform dispersion of alumina nanoparticles in the copper matrix. Another study by Wei et al. investigated the microstructure and mechanical properties of copper–alumina nanocomposites synthesized by electrodeposition [26]. The authors found that the incorporation of alumina nanoparticles improved the hardness and wear resistance of the copper matrix, as well as its thermal stability. The crystallite size of nanoparticles in a nanocomposite can be determined using various techniques, including X-ray diffraction (XRD) and transmission electron microscopy (TEM). The Williamson–Hall method is a commonly used technique to calculate the crystallite size from the XRD peak broadening. The crystallite size of copper nanoparticles in a copper–alumina nanocomposite synthesized by mechanical milling was investigated [27]. The crystallite size of copper nanoparticles decreased with increasing milling time, indicating the formation of nanocrystalline copper. The authors attributed the decrease in crystallite size to the deformation, cold welding, and fracturing of the powder particles during milling. The morphology of nanoparticles in a nanocomposite has attracted a great deal of attention due to its unique properties such as high strength, low density, and improved thermal and electrical conductivity [28–32]. Among various nanocomposite materials, copper-based nanocomposites have gained significant interest due to their unique combination of properties such as high electrical and thermal conductivity, high strength, and corrosion resistance. Copper-based nanocomposites can be prepared by various methods such as powder metallurgy, electrodeposition, and mechanical alloying.

Alumina ( $\text{Al}_2\text{O}_3$ ) is widely used as a reinforcement material due to its high strength, stiffness, and wear resistance [33,34]. The addition of alumina particles to copper matrices can improve their mechanical properties, such as strength, hardness, and wear resistance. In addition, alumina particles can improve the thermal stability and corrosion resistance of copper matrices. Therefore, the development of copper–alumina nanocomposites has been of great interest in recent years. The utilization of design of experiments (DOE) allows for a reduction in the number of experiments conducted, making it a practical method to identify effective parameters. Response surface methodology (RSM), as a type of DOE approach, enables the evaluation of multiple input parameters to determine the necessary experiments for obtaining desired responses [35,36].

Several studies have been reported on the synthesis and characterization of copper–alumina nanocomposites by mechanical alloying. For example, Kumar et al. [37] synthesized copper–alumina nanocomposites by mechanical alloying and subsequent hot-pressing. They found that the addition of alumina particles to copper matrices improved their hardness and wear resistance. Moreover, they observed that the alumina particles were uniformly dispersed in the copper matrix. The effect of alumina content on the microstructure and mechanical properties of copper–alumina nanocomposites synthesized by mechanical alloying was assessed. The addition of alumina particles increased the hardness and compressive strength of copper matrices [13,38]. Furthermore, the microstructure of the nanocomposites was composed of copper grains and dispersed alumina particles. Korać et al. synthesized copper–alumina nanocomposites by mechanical alloying and subsequent sintering [14]. They investigated the effect of milling time on the microstructure

and mechanical properties of the nanocomposites. They found that the nanocomposites exhibited a higher hardness and compressive strength compared to pure copper. Moreover, they observed that the alumina particles were homogeneously dispersed in the copper matrix. Two methods are used to prepare Cu-20 vol% Al<sub>2</sub>O<sub>3</sub> nanocomposite powders via high-energy planetary fast milling: solid solution and direct mixing. In the solid solution method, CuO powder is added to the Cu–Al solid solution powder, and the composite is fabricated by milling after 100 h. In the direct mixing method, Cu and Al<sub>2</sub>O<sub>3</sub> powders are mechanically milled via high-energy planetary fast milling for 100 h. Both methods produce nanocomposites with Al<sub>2</sub>O<sub>3</sub> nanoparticles in crystalline Cu matrices, but the solid solution method results in higher density and bending strength [39]. Another study focused on the fabrication and investigation of alumina-based nanocomposite powders reinforced with aluminum particles. The powders were milled for up to 30 h in a planetary ball mill to produce Al<sub>2</sub>O<sub>3</sub>–20% Al nanocomposite, and a uniform distribution of the aluminum reinforcement in the alumina matrix was successfully obtained after milling the powders. The crystal size decreased while the internal strain increased with the prolongation of milling times. The sintered composite exhibited decreased hardness but improved fracture toughness after adding aluminum to alumina. The maximum relative density was obtained at 1500 °C. The study highlights the potential application of Al<sub>2</sub>O<sub>3</sub>–20% Al nanocomposites in various industries due to their improved mechanical properties [40].

The present study combines design of experience (DoE), simulation of properties and experimental synthesis to investigate the design and characterization of a copper–alumina nanocomposite. Through the application of mechanical milling, a nanocomposite powder was successfully synthesized. The morphological and structural properties of the nanocomposite were analyzed using techniques such as SEM, TEM, and XRD. The TEM analysis confirmed the presence of alumina particles in the copper matrix, indicating the successful synthesis of the nanocomposite. XRD analysis revealed changes in the crystallite size of copper, attributed to the mechanical milling process. Additionally, simulation studies were conducted to further understand the behavior of the nanocomposite. The integration of experimental and simulation approaches provides a comprehensive understanding of the nanocomposite's properties, and opens up possibilities for its application in various fields. The findings from this study contribute to the advancement of nanocomposite design and provide a foundation for future research in this area.

## 2. Experimental Work and Design of Experiments

### 2.1. Production of Copper–Aluminum Solid Solution

This article focuses on the preparation of a copper–alumina nanocomposite with 20% alumina through the synthesis of copper–alumina nanocomposite powder from copper and aluminum oxide raw materials, while also investigating the regeneration reaction that occurs during the grinding of the mixed powders in a planetary mill. To create the desired final product, copper, aluminum, and copper oxide powders were prepared, each with specific properties. The copper powder used had a purity of over 99.7% and a particle size smaller than 63 µm (Rahway, NJ, USA, Merck, Art. No. 2715). The copper oxide powder used had a purity of over 96% and a particle size smaller than 160 µm (Merck, Art. No. 2761). The aluminum powder had a purity of over 99.9% and a particle size smaller than 50 µm (Merck, Art. No. 1056).

To produce the nanocomposite, it was necessary to avoid direct grinding of the mixture of copper oxide powders (bivalent) and aluminum metal powder, as this process is extremely exothermic and may lead to explosion in the mill. To overcome this problem, various methods are available, including the production of copper–aluminum solid solution, the production of copper–aluminum intermetallic compounds, or the addition of extra copper to the stoichiometric composition. This article employed the production of copper–aluminum solid solution as a solution to this problem. Previous studies have shown that the mechanical alloying of copper and aluminum powders in an atomic ratio of copper to aluminum of 6:1 results in the formation of a copper–aluminum solid solution [41,42].

The weight ratio of copper–alumina nanocomposite components was determined using the two-component phase equilibrium diagram of copper–aluminum in terms of atomic percentage and weight percentage, as shown in Figure 1.

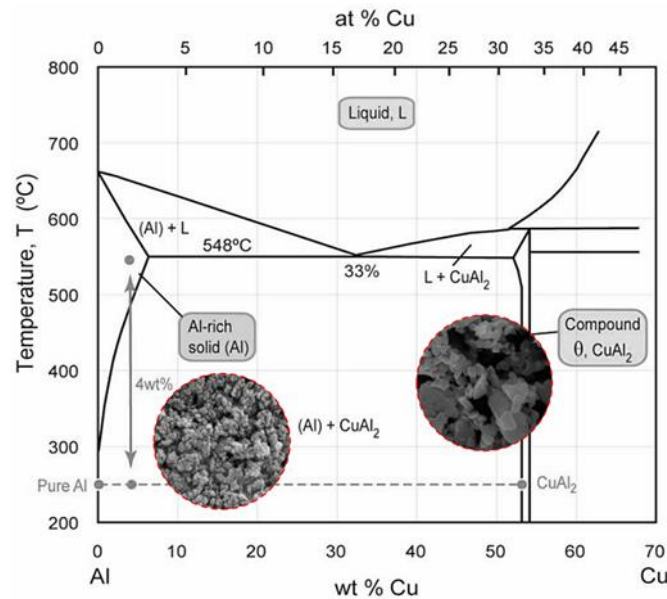


**Figure 1.** Al–Cu equilibrium phase diagram.



The atomic ratio of copper to aluminum is 6 to 1. The weight ratio of the constituent components was determined based on the chemical characteristics of the material, considering the presence of 20% alumina in the final powder and using Equation (1). Due to the limitation of the mill bag, the total weight of the mixed powders was 10 g. Knowing the weight percentage of the raw materials, the weight of each component in the 10 g mixture was easily calculated. The copper–aluminum solid solution was prepared by milling copper and aluminum powders at the stoichiometric composition of the formula for 10, 20, 30, 40 and 50 h using a planetary mill. A grinder consisting of two cups made of stainless Fritsch model with a volume of 250 cubic centimeters and six steel balls with a diameter of 20 mm and a rotation speed of the mill of 275 rpm were used for the powder mixture milling. The bullet weight ratio was 23.26 during the milling process, and the powders were ground at different times to investigate the phases using X-ray diffraction (XRD) patterns and to ensure the formation of solid solution while performing thermal analysis (STA). The phase analysis was performed using an X-ray diffraction device manufactured by Siemens, and simultaneous thermal analysis was carried out using the STA model 1640 device of Polymer Laboratories, Shropshire, UK.

## 2.2. Production of Copper–Alumina Nanocomposite

Following the attainment of equilibrium in the mill reaction between copper and aluminum powders for 50 h, divalent copper oxide powder was added to the solid solution in a stoichiometric amount. The entire powder mixture was subsequently subjected to milling for a period of 20, 40, 60, 80 and 100 h using a planetary mill. The new powder mixture was then milled under identical conditions as before, albeit with a ball to powder ratio of 18. Similar to the prior case, the reason for the sequential grinding of the powder mixture at distinct intervals was to conduct phase investigation with the aid of patterns for simultaneous thermal analysis (STA) and X-ray diffraction (XRD), in order to ascertain the formation of a copper–alumina composite. Figure 2 shows the schematic and actual ball milling chamber.

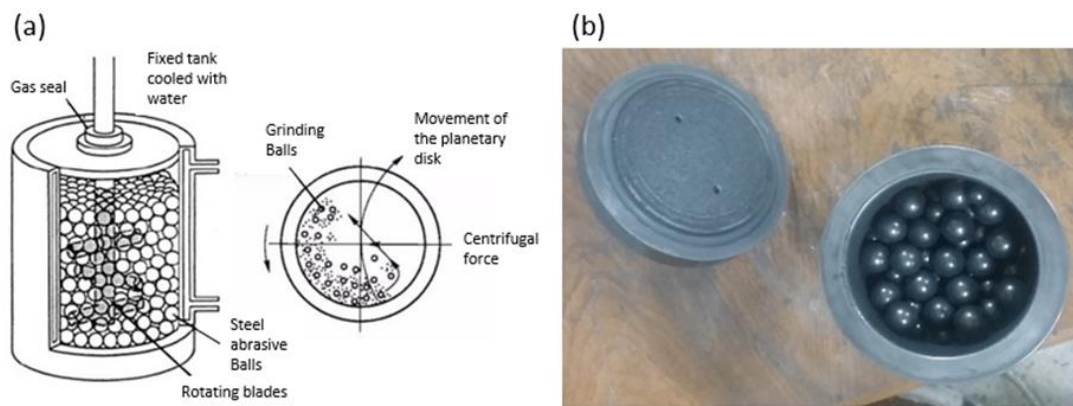


**Figure 2.** (a) Schematic view of ball milling chamber with details, (b) actual chamber prepared for this study.

### 2.3. Methods of Characterization

The nanocomposite powder that was synthesized was subjected to microstructure examination using a scanning electron microscope (SEM) MIRA3-TESCAN, Czech Republic. SEM images were taken to analyze the morphology of the nanocomposite powder particles obtained after milling for 20, 40, 60, 80 and 100 h. Additionally, the particle size of the nanocomposite powder was investigated by taking pictures with a transmission electron microscope (PHILIPS-CM 200 FEG model).

## 3. Results and Discussion

### 3.1. Statistical Results and Optimization

The results obtained from the conducted experiment are presented and discussed in this section. The experiment focused on investigating the effects of milling time and temperature on particle size and the differential thermal response ( $\Delta t. \mu V$ ). The experimental design employed a set of input variables, including milling time (h) and temperature ( $^{\circ}C$ ), and measured the corresponding output variables, namely, particle size (nm) and differential thermal response ( $\Delta t. \mu V$ ). The obtained data are summarized in Table 1.

**Table 1.** Experimental design and results.

Experimental No.	Input Variables		Output Variables	
	Milling Time (h)	Temperature ( $^{\circ}C$ )	Particle Size (nm)	Differential Thermal ( $\Delta t. \mu V$ )
1	20	500	$57 \pm 3$	$58 \pm 2$
2	30	1000	$47 \pm 2$	$55 \pm 3$
3	40	1500	$40 \pm 5$	$52 \pm 2$
4	50	500	$36 \pm 4$	$34 \pm 1$
5	60	1000	$32 \pm 3$	$28 \pm 3$
6	70	1500	$24 \pm 6$	$23 \pm 3$
7	80	500	$19 \pm 3$	$21 \pm 2$
8	90	1000	$9 \pm 2$	$21 \pm 3$
9	100	1500	$5 \pm 3$	$19 \pm 1$

The experimental design comprised nine different combinations of milling time and temperature settings. Each set of input variables was associated with specific values of particle size and the differential thermal response ( $\Delta t. \mu V$ ). These measurements provide valuable insights into the influence of milling time and temperature on the resulting particle size and thermal characteristics of the material. In the subsequent sections, the results will be analyzed and discussed to determine the relationship between the input variables and the output variables. The statistical analysis, including analysis of variance (ANOVA) and regression analysis, will be performed to assess the significance of the observed trends, and

quantify the effects of milling time and temperature on particle size and the differential thermal response. Furthermore, the findings will be compared to the existing literature and theoretical models to gain a comprehensive understanding of the observed phenomena.

### 3.1.1. Particle Size

A statistical analysis of the data using analysis of variance (ANOVA) was conducted to examine the significance of the factors and their interactions in relation to the particle size output variable. The results of the ANOVA are summarized in Table 2. Equation (2) in terms of actual factors can be used to make predictions about the response for given levels of each factor.

**Table 2.** ANOVA results for particle size.

Source	Sum of Squares	df	Mean Square	F-Value	p-Value
Model	2369.08	5	473.82	120.42	0.0012
A-Milling Time	1218.91	1	1218.91	309.78	0.0004
B-Temperature	0.5297	1	0.5297	0.1346	0.7380
AB	5.97	1	5.97	1.52	0.3058
A <sup>2</sup>	2.98	1	2.98	0.7577	0.4481
A <sup>2</sup> B	1.44	1	1.44	0.3666	0.5876
Residual	11.80	3	3.93		
Cor Total	2380.89	8			
R-Squared = 95.50%				R-Squared (Adj) = 93.71%	

$$\text{Particle Size} = +76.15466 - 0.781436\text{Milling Time} - 0.014354\text{Temperature} + 0.000339\text{Milling Time} \times \text{Temperature} + 0.000574\text{Milling Time}^2 \quad (2)$$

The analysis indicates that the overall model is significant, as evidenced by the low *p*-value (0.0012). Figure 3a indicates that the combined effects of the factors A (Milling Time), B (Temperature), AB, A<sup>2</sup>, and A<sup>2</sup>B significantly contribute to explaining the variations observed in the particle size. The individual factor A (Milling Time) is found to be highly significant, with a very low *p*-value (0.0004) and a large F-value (309.78). This suggests that Milling Time has a substantial influence on the particle size. However, the factor B (Temperature) is not found to be significant, as indicated by the relatively high *p*-value (0.7380) and the small F-value (0.1346). Thus, Temperature does not have a significant impact on the particle size in this experimental setup. The interaction term AB, and the quadratic terms A<sup>2</sup> and A<sup>2</sup>B, are also not found to be significant, as their *p*-values are relatively high and their corresponding F-values are relatively small. This suggests that the interactions between Milling Time and Temperature (AB) and the squared terms of Milling Time (A<sup>2</sup>) and A<sup>2</sup> multiplied by B (A<sup>2</sup>B) do not have a significant impact on the particle size. The levels should be specified in the original units for each factor. This equation should not be used to determine the relative impact of each factor because the coefficients are scaled to accommodate the units of each factor and the intercept is not at the center of the design space (Figure 3b).

Figure 4a,b shows that factor A (Milling Time) exhibits high significance with a very low *p*-value (0.0004) and a large F-value (309.78), suggesting its substantial influence on particle size. However, factor B (Temperature) is not found to be significant, as indicated by the relatively high *p*-value (0.7380) and small F-value (0.1346). Thus, Temperature does not have a significant impact on the particle size in this experimental setup. The interaction term AB, as well as the quadratic terms A<sup>2</sup> and A<sup>2</sup>B, are also not found to be significant, as reflected by their relatively high *p*-values and small F-values. This suggests that the interactions between Milling Time and Temperature (AB) and the squared terms of Milling Time (A<sup>2</sup>) and A<sup>2</sup> multiplied by B (A<sup>2</sup>B) do not have a significant impact on the particle size.

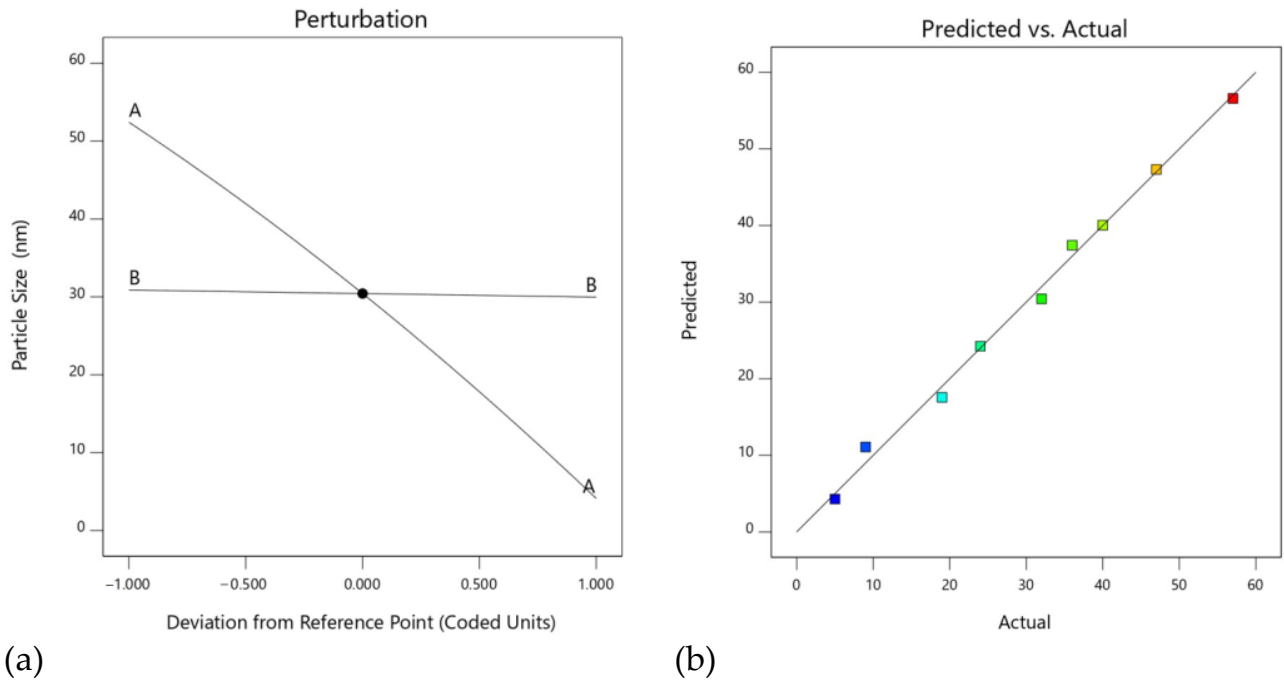


Figure 3. (a) Perturbation relationship plot; (b) predicted versus actual plot for particle size.

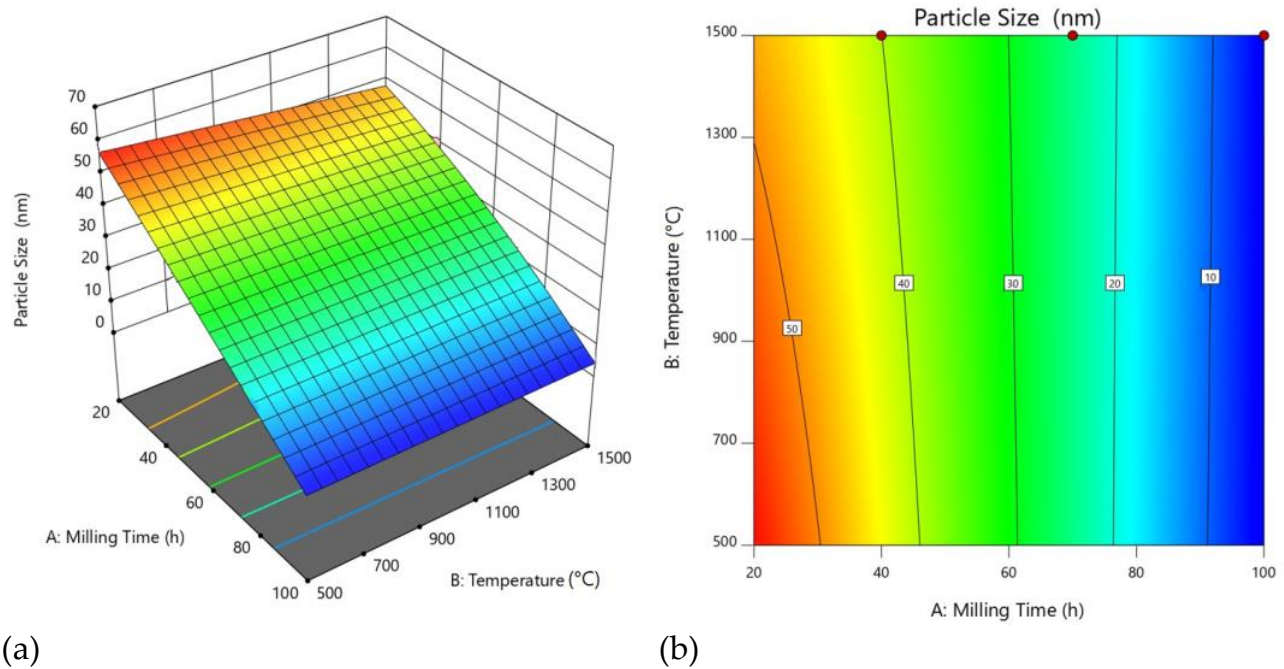


Figure 4. (a) Surface and (b) contour plots for correlation between particle size, temperature and milling time.

### 3.1.2. Differential Thermal Response

The statistical analysis of the data using analysis of variance (ANOVA) was conducted to examine the significance of the factors and their interactions in relation to the output variable of Differential Thermal response ( $\Delta t.\mu V$ ). The results of the ANOVA are summarized in Table 3 and Equation (3).

**Table 3.** ANOVA results for differential thermal ( $\Delta t, \mu V$ ).

Source	Sum of Squares	df	Mean Square	F-Value	p-Value
Model	2041.11	5	408.22	71.57	0.0026
A—Milling Time	1802.67	1	1802.67	316.05	0.0004
B—Temperature	36.82	1	36.82	6.45	0.0846
AB	57.75	1	57.75	10.13	0.0500
A <sup>2</sup>	174.22	1	174.22	30.55	0.0117
A <sup>2</sup> B	0.5401	1	0.5401	0.0947	0.7784
Residual	17.11	3	5.70		
Cor Total	2058.22	8			
R-Squared = 99.17%			R-Squared (Adj) = 97.78%		

$$\text{Differential Thermal} = +76.48148 - 1.47407\text{Milling Time} + 0.021815 \text{ Temperature} - 0.000348\text{Milling Time} \times \text{Temperature} + 0.010370\text{Milling Time}^2 \quad (3)$$

The analysis in Figure 5 indicates that the overall model is significant, as evidenced by the low *p*-value (0.0026). This suggests that the combined effects of the factors A (Milling Time), B (Temperature), AB, A<sup>2</sup>, and B<sup>2</sup> significantly contribute to explaining the variations observed in the differential thermal response. The individual factor A (Milling Time) is found to be highly significant, with a very low *p*-value (0.0004) and a large F-value (316.05). This indicates that Milling Time has a substantial influence on the differential thermal response. The factor B (Temperature) is not found to be significant, as indicated by the relatively high *p*-value (0.0846) and the moderate F-value (6.45). Thus, Temperature does not have a significant impact on the differential thermal response in this experimental setup. The interaction term AB is not found to be significant, as its *p*-value (0.0500) is relatively high and the F-value (10.13) is moderate. Figure 6a,b show that the interaction between Milling Time and Temperature (AB) does not have a significant impact on the differential thermal response. The quadratic term A<sup>2</sup> is found to be significant, with a low *p*-value (0.0117) and a relatively large F-value (30.55). This suggests that the squared term of Milling Time (A<sup>2</sup>) has a significant influence on the differential thermal response.

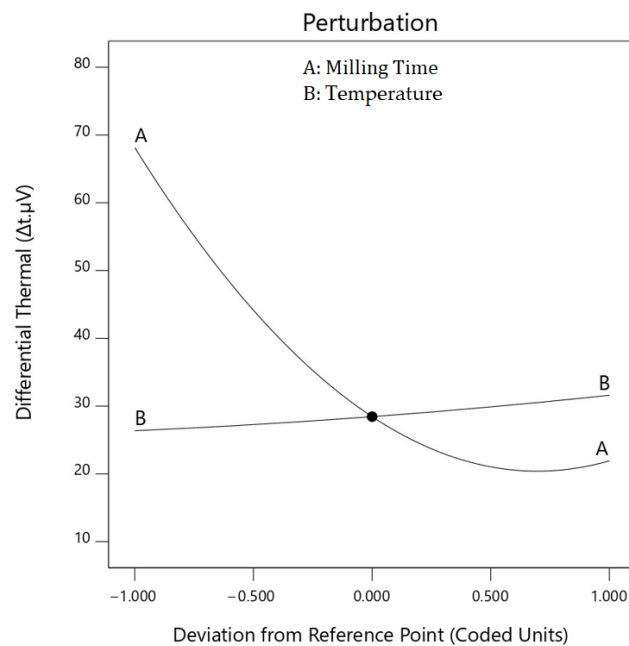


**Figure 5.** Perturbation relationship plot for differential thermal.

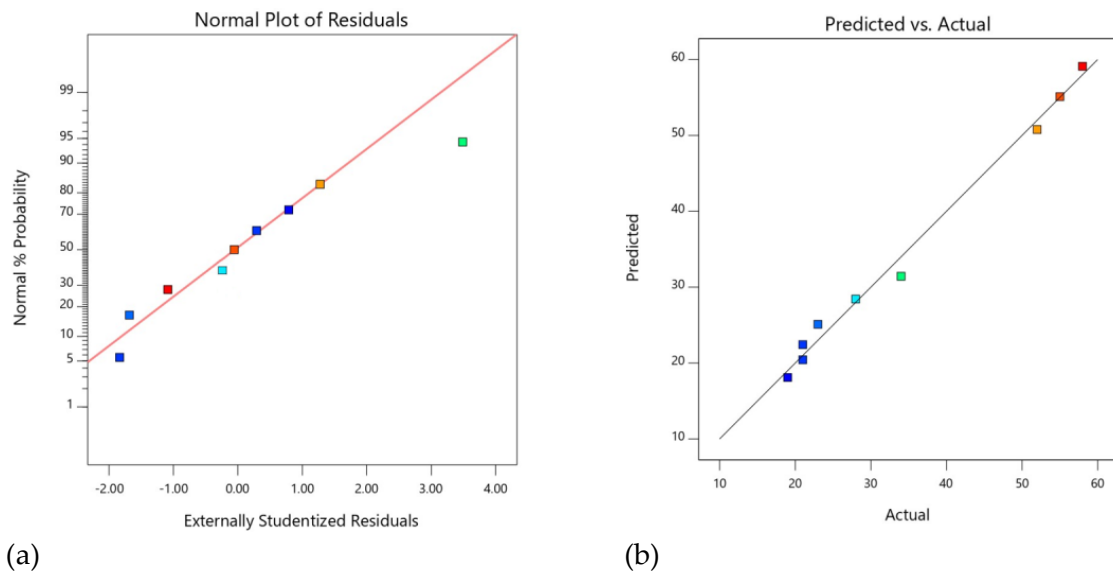


**Figure 6.** (a) The normal plot of residuals (b) predicted versus actual plot for differential thermal as the output variable.

On the other hand, the quadratic term  $B^2$  is not found to be significant, as its  $p$ -value (0.7784) is relatively high and the  $F$ -value (0.0947) is small. This indicates that the squared term of Temperature ( $B^2$ ) does not have a significant impact on the differential thermal response.

The analysis of the surface plot, as shown in Figure 7a,b, indicates the significance of the overall model, supported by the low  $p$ -value (0.0026). This suggests that the combined effects of factors A (Milling Time), B (Temperature), AB,  $A^2$ , and  $B^2$  significantly contribute to explaining the variations observed in the differential thermal response.

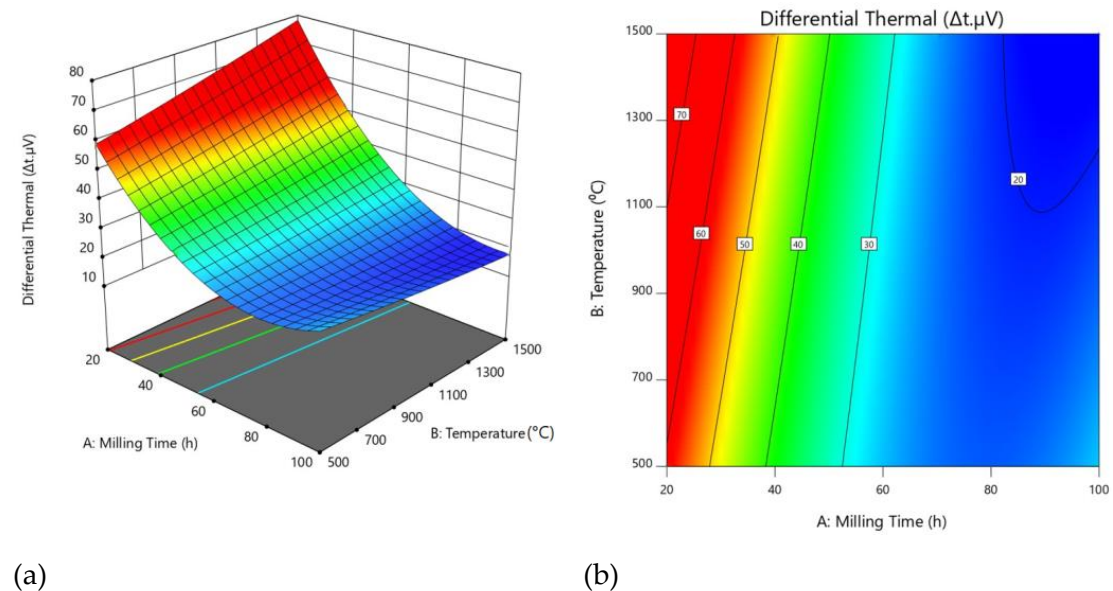


**Figure 7.** (a) Surface and (b) contour plots for correlation between differential thermal, temperature and milling time.

### 3.1.3. Optimization

The goal of the optimization process was to find solutions that satisfy the given constraints while optimizing the response variables, specifically particle size and differential thermal, within their respective ranges. The constraints for the input variables (Milling Time and Temperature) and output variables (particle size and differential thermal) are presented in Table 4.

**Table 4.** Optimization constraints.

Name	Goal	Lower Limit	Upper Limit	Lower Weight	Upper Weight	Importance
A: Milling Time	is in range	20	100	1	1	3
B: Temperature	is in range	500	1500	1	1	3
Particle Size	is in range	5	57	1	1	3
Differential Thermal	is in range	19	58	1	1	3

A total of 100 solutions were found during the optimization process. The solutions are listed in Table 5, along with their corresponding values for Milling Time, Temperature, particle size, differential thermal, and desirability.

**Table 5.** Optimization solutions.

Number	Milling Time (h)	Temperature (°C)	Particle Size (nm)	Differential Thermal ( $\Delta t, \mu V$ )	Desirability
1	86.011	1276.340	13.976	19.537	1.000
2	40.000	1500.000	40.037	50.778	0.987
3	50.000	500.000	37.424	31.444	0.965

The optimization process successfully identified solutions that meet the constraints for the input variables and fall within the desired ranges for particle size and differential thermal. These solutions exhibit a high desirability of 1.000, indicating that they are optimal. Solution 1 corresponds to a Milling Time of 86.011, Temperature of 1276.340, particle size of 13.976, and differential thermal of 19.537. Solution 2 has a Milling Time of 40.000, Temperature of 1500.000, particle size of 40.037, and differential thermal of 50.778. Solution 3 exhibits a Milling Time of 50, Temperature of 500, particle size of 37.424, and differential thermal of 31.444. As shown in Figure 8, these solutions provide viable combinations of input variables that satisfy the constraints while achieving desired levels of the output variables. The optimization process offers valuable insights for selecting appropriate parameter values to achieve the desired particle size and differential thermal responses within the specified ranges.

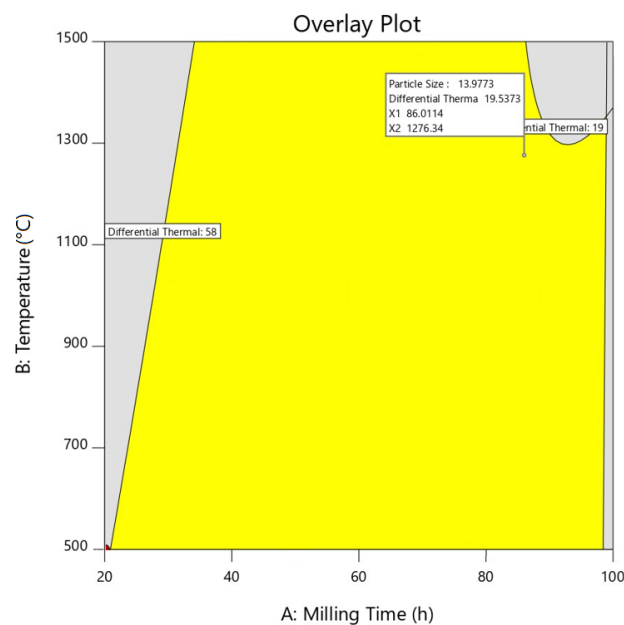


**Figure 8.** Overlay plot for temperature and milling time.

### 3.2. Alloying Simulation

#### 3.2.1. Phase Detection

The phase analysis of the copper–aluminum system was conducted using the copper–aluminum phase diagram, which provides valuable insights into the compounds formed at different temperature ranges (Figure 9). The diagram encompasses the entire temperature range and highlights the formation of various phases. Among the notable phases identified in this system are the critical intermetallic compounds  $\text{Al}_2\text{-Cu}$  and various forms of  $\text{Al-Cu}$ . These compounds play a significant role in understanding the behavior and properties of copper–aluminum alloys. The crystal structure of these phases is also specified, providing further details regarding their atomic arrangement and bonding characteristics. The composition of the alloy studied in this analysis is specified as  $\text{Al} = 20\%$ ,  $\text{Cu} = 80\%$ , and trace amounts of oxygen (O). This composition represents a specific alloy composition within the copper–aluminum system, allowing for a focused investigation of the phases formed at the given temperature range. The temperature range considered in this study spans from  $0\text{ }^\circ\text{C}$  to  $1500\text{ }^\circ\text{C}$ , encompassing a wide range of thermal conditions that can influence phase formation and stability.

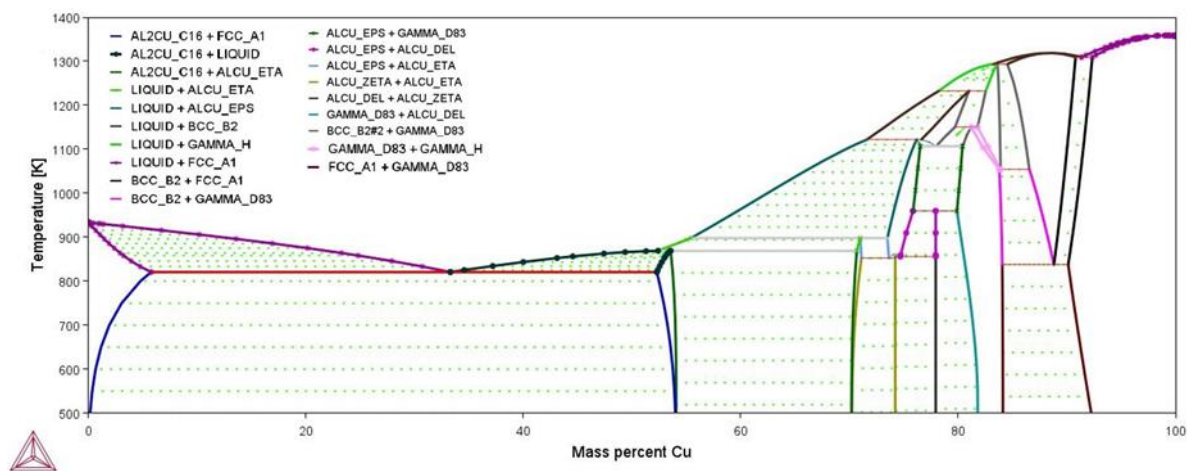


**Figure 9.** Phase detection diagram reproduced by Thermo Calculator.

This broad temperature range enables a comprehensive understanding of the phase behavior and transformations in the copper–aluminum system. It is important to note that the data used for this analysis were obtained from the Thermo Calculator Software, a reliable tool commonly used for phase diagram calculations and predictions. The software provides accurate and reliable information on the formation of phases within the copper–aluminum system, contributing to the overall understanding of the alloy’s phase diagram and its practical implications. By utilizing the copper–aluminum phase diagram and incorporating data from Thermo Calculator Software, this study provides a comprehensive analysis of the phases formed at different temperature ranges within the copper–aluminum system. Understanding the phase behavior and composition of copper–aluminum alloys is crucial for their application in various industries, and this analysis contributes valuable information towards that goal.

#### 3.2.2. Alloy Properties Prediction

The electrical and thermal properties of a copper–aluminum alloy with a composition of  $\text{Cu} = 80\%$  and  $\text{Al} = 19.90\%$  up to  $20\%$ , including the presence of gas (oxygen), were investigated using JMatPro V7 software. The analysis was performed considering various phases and a fraction of liquid of 0.01, and all are shown in Figure 10.

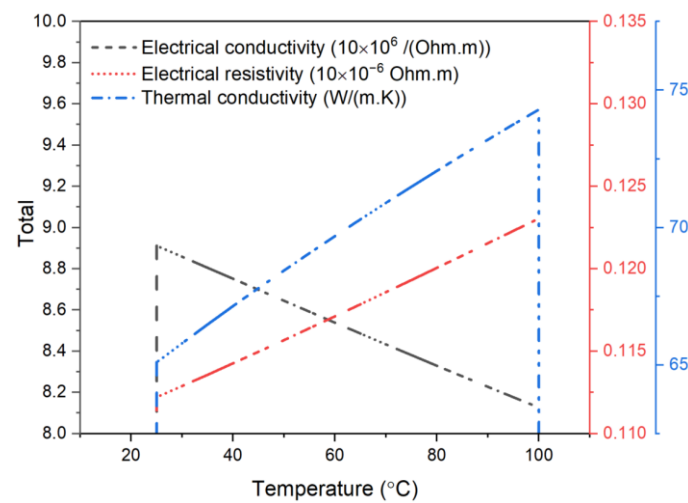


**Figure 10.** The electrical and thermal properties of a copper–aluminum alloy with a composition of Cu = 80% and Al = 20%, including the presence of gas (oxygen).

The temperature range of interest for this study is up to 100 °C, representing the environmental temperature conditions. The software simulated the electrical conductivity, electrical resistivity, and thermal conductivity of the alloy at different temperatures within this range. The results of the simulation indicate that the electrical conductivity of the copper–aluminum alloy decreases with decreasing temperature. At 100 °C, the electrical conductivity was found to be  $8.12686 \times 10^6$  1/(Ohmm), gradually decreasing to  $8.91189 \times 10^6$  1/(Ohmm) at 25 °C. This trend suggests that the alloy exhibits good electrical conductivity across the investigated temperature range. Conversely, the electrical resistivity of the alloy increases with decreasing temperature. At 100 °C, the electrical resistivity was measured as  $0.12305 \times 10^{-6}$  Ohmm, gradually increasing to  $0.11221 \times 10^{-6}$  Ohmm at 25 °C. This observation indicates that the alloy’s resistance to electrical flow increases as the temperature decreases. Regarding the thermal properties, the thermal conductivity of the alloy decreases with decreasing temperature. At 100 °C, the thermal conductivity was found to be 74.29715 W/(mK), gradually decreasing to 65.09843 W/(mK) at 25 °C. This trend suggests that the alloy exhibits relatively high thermal conductivity, indicating its ability to efficiently conduct heat.

The bulk modulus, shear modulus, and Young’s modulus of a copper–aluminum alloy were analyzed using JMatPro V7 software and are shown in Figure 11. The alloy composition consists of Cu = 80% and Al = 19.90% up to 20%, including the presence of gas (oxygen). The simulation was performed at temperatures ranging up to 100 °C.

The bulk modulus is a measure of a material’s resistance to uniform compression. The results show that the bulk modulus of the copper–aluminum alloy increases with decreasing temperature. At 100 °C, the bulk modulus was determined to be 99.92319 GPa, gradually increasing to 115.80375 GPa at 25 °C. This observation suggests that the alloy becomes stiffer and less compressible as the temperature decreases. The shear modulus represents a material’s resistance to shear deformation. Similar to the bulk modulus, the shear modulus of the alloy increases with decreasing temperature. At 100 °C, the shear modulus was measured as 38.38156 GPa, gradually increasing to 39.67642 GPa at 25 °C. This indicates that the alloy becomes more resistant to shear stress as the temperature decreases. Young’s modulus, also known as the elastic modulus, characterizes a material’s stiffness under tensile or compressive loads. The results reveal that the Young’s modulus of the copper–aluminum alloy increases with decreasing temperature. At 100 °C, the Young’s modulus was found to be 103.64313 GPa, gradually increasing to 106.82878 GPa at 25 °C. This indicates that the alloy exhibits greater stiffness and resistance to deformation as the temperature decreases.

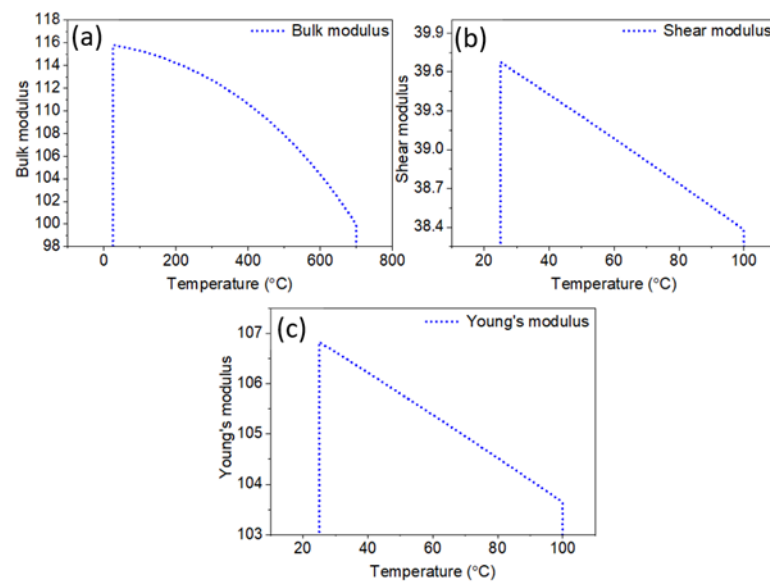


**Figure 11.** The (a) bulk modulus, (b) shear modulus, and (c) Young's modulus of a copper–aluminum alloy were analyzed using JMatPro V7 software.

### 3.3. Experimental Results

#### 3.3.1. Phase Identification by XRD

Based on the analysis of X-ray diffraction patterns, it was observed that with increasing the milling time of the copper–aluminum powder mixture to obtain a solid solution, the peaks shift towards lower  $2\theta$  degrees. This observation is depicted in Figure 12. The shift in peaks suggests that more aluminum atoms are being incorporated into the copper structure during the milling process. As aluminum occupies a position in the crystal lattice of copper, the lattice constant of copper increases. This, in turn, causes the XRD peaks to shift towards the left, indicating a decrease in  $2\theta$  degrees.

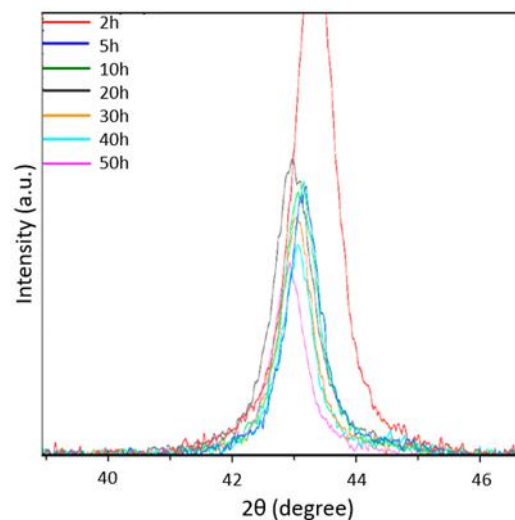


**Figure 12.** The diagram of the XRD peaks of the produced powder mixture.

According to the XRD pattern at 10 h, it is difficult to detect the peak for aluminum, suggesting that aluminum has already reacted with copper within the first 10 h of milling. A comparison of the peak of the pure copper plane (111) with the peak of the milled copper plane (111) after 50 h indicates a shift of  $2\theta$  from 43.39 degrees to 42.93 degrees (Figure 12), confirming the penetration of aluminum into the copper structure.

These findings demonstrate that the mechanical grinding of copper and aluminum powders (14 atomic %) produces a solid solution Cu (Al). As the milling time increases,

the intensity of the copper peaks decreases, indicating a reduction in the reaction rate. This can be attributed to a reduction in the amount of unreacted materials present in the milling process. Initially, the reaction rate is higher due to the larger quantity of reactants present in contact. However, as the reaction progresses, product phases are formed in the common phase between the reactants, leading to a decrease in the reaction rate [43]. The thermal analysis of samples milled at different times (differential DTA) was also conducted to confirm the formation of the copper–aluminum solid solution (Figure 13). The results of the differential DTA indicate the presence of a specific endothermic peak in the early stages of milling at a temperature of 550 °C, which is attributed to the solid-state reaction between copper and aluminum powders. As the milling time exceeds 10 h, the endothermic peak disappears, indicating that almost all aluminum has entered the copper structure.

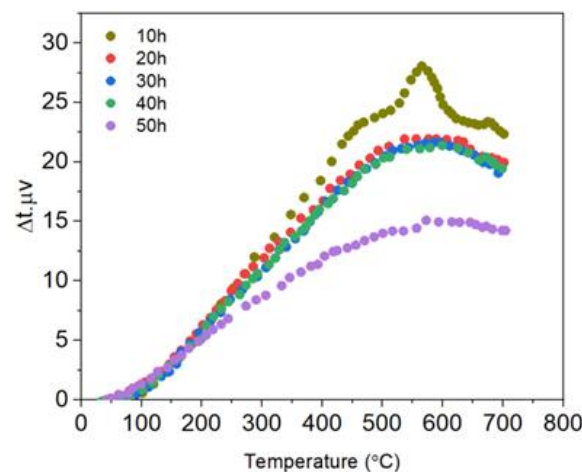


**Figure 13.** Differential thermal analysis (DTA) graphs of copper–aluminum solid solution at different milling times.

The Cu (Al) plane (111) peak of copper in the solid solution is shifted to the left by around 43 degrees, indicating that aluminum has been removed from the copper structure. However, there is still some aluminum left in the structure, as evidenced by the small difference in the peak position. The appearance of alumina peaks in the XRD pattern of the resulting nanocomposite can be attributed to the presence of alumina in the structure. The absence of the diffraction angle of copper in the nanocomposite with pure copper suggests that aluminum is not completely removed from the copper structure.

The results of the differential thermal analysis (DTA) shown in Figure 14 confirm the end of the reaction. The initial endothermic peaks observed at different temperatures in the early stages of milling can be attributed to the release of copper from the solid solution, while the higher temperature peak is due to the formation of alumina. It should be noted that the reason for continuing the milling process for longer times is to achieve a finer nanocomposite powder and to ensure a complete reaction. The shift of the XRD diffraction peaks to the right with increasing milling time indicates that the reaction is progressing and more peaks are shifting towards the right with increasing milling time.

The size of copper particles in copper–alumina nanocomposite was calculated using the Williamson–Hall formula (Equation (4)) as follows:

$$B \cos\theta = \frac{K\lambda}{d} + 2\eta \sin\theta \quad (4)$$

where  $\lambda = 0.15406$  nm is wavelength of the X-ray,  $K$  is the coefficient equal to 0.89,  $d$  is the crystallite size,  $\theta$  is the Bragg angle,  $\eta$  is the internal strain and  $B$  is the peak width at half maximum intensity (FWHM).

Additionally, peak broadening can also be affected by instrumental broadening, which is related to the characteristics of the X-ray diffractometer and the X-ray source used. In

order to accurately determine the crystallite size, other techniques such as transmission electron microscopy (TEM) or scanning electron microscopy (SEM) can also be used. These techniques provide the direct visualization of the particle size and shape, which can be used to determine the crystallite size more accurately.

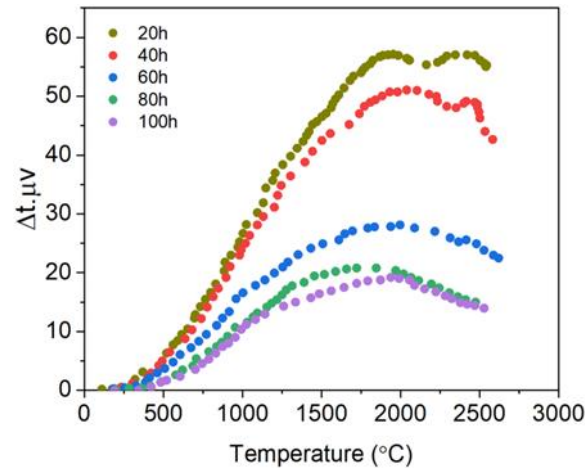


**Figure 14.** The results of the differential thermal analysis (DTA) of nanocomposite powder at different times.

### 3.3.2. The Microstructure of the Produced Nano Powder

Nanocomposite materials have attracted significant attention in recent years due to their unique properties and potential applications. These materials consist of a matrix material, usually a metal or an alloy, in which nanoparticles or other nanoscale reinforcements are dispersed. One approach to synthesizing nanocomposites involves mechanical milling, which involves grinding the materials in a ball mill for an extended period to achieve the desired particle size and distribution. In this context, it is important to note that the properties of nanocomposite materials are highly dependent on the particle size and distribution of the constituent materials. As such, it is essential to carefully monitor the morphological changes that occur during the milling process to ensure that the desired properties are achieved. One common issue encountered during the milling of nanocomposite materials is the formation of larger copper particles due to the soft nature of the metal. Specifically, as the copper grains are ground, they tend to stick together and form larger particles via welding. This phenomenon can be detrimental to the quality of the resulting nanocomposite material, as it can lead to the poor distribution of the reinforcement particles and other defects. To address this issue, researchers have explored the use of process control agents to prevent particle welding and enhance the dispersion of the reinforcement particles. However, it is important to note that the use of such agents can introduce unwanted contaminants into the resulting powder, which can affect the final properties of the material. Therefore, in some cases, researchers opt not to use process control agents to avoid contamination and achieve higher purity in the resulting powder. Furthermore, the morphology of the nanocomposite powder can also be influenced by the weight percentage of the reinforcement particles and their size. In some cases, the size of the reinforcement particles may be so small that it is difficult to identify them using traditional characterization techniques, such as scanning electron microscopy (SEM). Additionally, SEM images may only display surface features of the particles, which can further complicate their identification.

To investigate the morphology of the resulting nanocomposite powder, researchers often perform milling for different lengths of time, and monitor the changes in particle shape and size. For instance, in this study, the morphology of the nanocomposite powder was investigated after milling for 20, 40, 60, 80 and 100 h. After 20 h of milling, the powder particles were found to be partially cold-boiled, while after 40 h, the cold-boiled particles became sheets due to collisions with the pellets. Finally, after 60 h of milling,

all the powder particles were found to be in the form of sheets, as observed via SEM in Figure 15. It is worth noting that the grinding process can lead to partial spheroidization and separation of the powder particles. However, complete separation and spheroidization can require additional milling time to achieve the desired morphology and distribution of the reinforcement particles. The microstructure of a copper-based nanocomposite was investigated, with a focus on the copper grains and alumina particles dispersed throughout the material. Crystallite size was determined using the Williamson–Hall method, and it was found that the TEM-derived size was smaller than that obtained from natural subject images. TEM imaging with a bright background revealed the presence and size of alumina particles in the nanocomposite, as indicated by differences in the thickness of various parts of the powder. The use of a dark background further confirmed the presence of two different phases in the nanocomposite. The TEM analysis of different regions within the dark background images shows the presence of alumina particles in the copper background, as well as the presence of carbon and nickel peaks due to the use of the powder holding net.

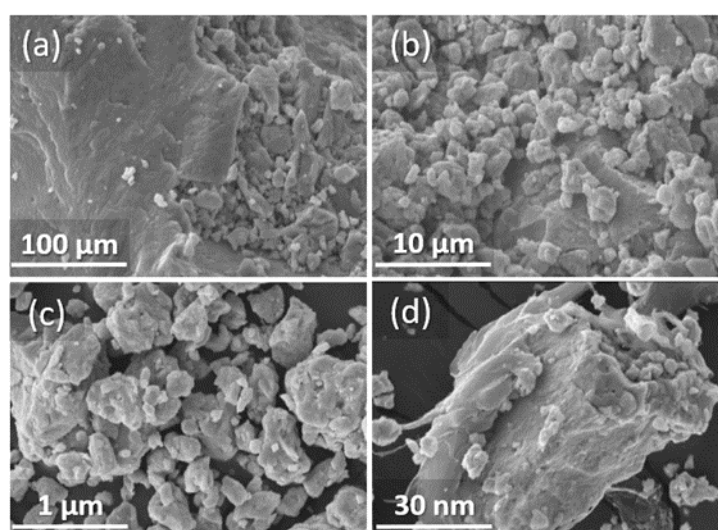


**Figure 15.** SEM images of final nanocomposite powder after 100 h of milling (a–d) all same SEM images in different magnifications.

Two distinct sizes of alumina particles were observed in the nanocomposite, with sizes of 40–10 nm and 20–5 nm, as determined by TEM imaging (Figure 16). The distribution of these two particle sizes suggests that coarse particles were formed in the initial stages of synthesis through mechanical grinding and high temperatures, while fine particles were produced at later stages and lower temperatures at controlled speeds. It is worth noting that the presence of all fine particles cannot be attributed solely to the breaking down of coarse particles, as a more uniform distribution of particle size would be expected if this were the case.

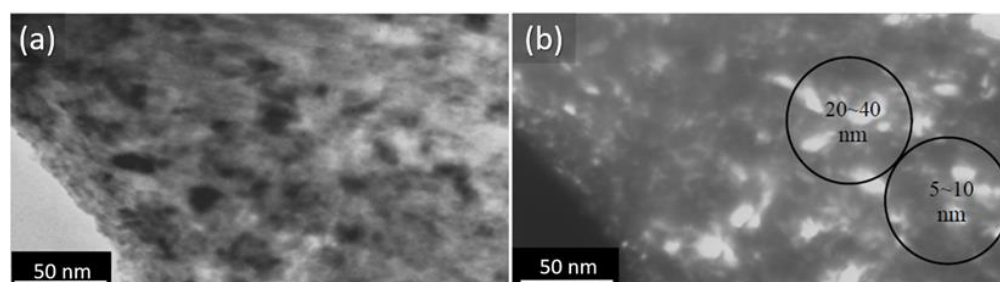


**Figure 16.** TEM images of the produced nanocomposite (a) in white background (b) in black background.

#### 4. Conclusions

Nanocomposite materials have garnered significant attention in recent years due to their unique properties and potential applications in various fields. Among the various methods of synthesis, mechanical milling has emerged as a promising technique for producing nanocomposite powders with enhanced mechanical properties. In this study, a nanocomposite powder was synthesized using the mechanical milling technique with copper as the base material and alumina as the reinforcing phase. The morphological and structural characterization of the synthesized powder was done using various techniques such as SEM, TEM, and XRD. Based on the results obtained from the characterization techniques, it can be concluded that the mechanical milling technique is an effective method for producing nanocomposite powders with improved mechanical properties. The key findings of the study can be summarized as follows:

1. The presence of alumina particles in the copper background was observed through TEM analysis, and the distribution of two sizes of alumina particles indicates the formation of coarse particles in the initial stages of synthesis and fine particles in later stages;
2. XRD analysis revealed a decrease in the crystallite size of copper with increasing milling time, which can be attributed to the formation of defects in the crystal lattice due to the milling process;
3. The SEM images show the separation and partial spheroidization of the powder particles during the milling process, leading to the formation of sheets after 60 h of milling;
4. The absence of nano-copper particles in the synthesized powder was observed through SEM analysis due to the low weight percentage of alumina in the nanocomposite powder.
5. The findings suggest that the mechanical milling technique could have potential applications in the development of advanced materials for various industries;
6. The impact of milling time and temperature on particle size was analyzed using RSM. Among the two input parameters, it is observed that milling time has a greater influence on particle size compared to temperature. This is evident from the lower coefficient of the temperature variable in the regression equation.
7. Out of the three optimal samples, the combination of 40 h of milling time and a temperature of 1500 °C resulted in a particle size of 40.037 nm and a differential thermal value of 50.778  $\Delta t.$  $\mu V$ .

**Author Contributions:** Conceptualization, M.R., M.K. and M.B.; investigation, simulation, O.A. and M.R.; formal analysis, M.K. and M.B.; writing—original draft, M.R. and M.K.; writing—review and editing, M.R., M.K. and M.B.; visualization, M.R. and M.K. All authors have read and agreed to the published version of the manuscript.

**Funding:** This research received no external funding.

**Data Availability Statement:** Not applicable.

**Acknowledgments:** The authors would like to express their gratitude to the developers of JMatPro V7 software for providing the necessary tools and resources for conducting the simulations and obtaining the data used in this analysis.

**Conflicts of Interest:** The authors declare no conflict of interest.

#### References

1. Raab, S.J.; Guschlbauer, R.; Lodes, M.A.; Körner, C. Thermal and Electrical Conductivity of 99.9% Pure Copper Processed via Selective Electron Beam Melting. *Adv. Eng. Mater.* **2016**, *18*, 1661–1666. [[CrossRef](#)]
2. Rezayat, M.; Karamimoghadam, M.; Yazdi, M.S.; Moradi, M.; Bodaghi, M. Statistical Analysis of Experimental Factors for Synthesis of Copper Oxide and Tin Oxide for Antibacterial Applications. *Int. J. Adv. Manuf. Technol.* **2023**, *127*, 3017–3030. [[CrossRef](#)]

3. Afonnikova, S.D.; Veselov, G.B.; Bauman, Y.I.; Gerasimov, E.Y.; Shubin, Y.V.; Mishakov, I.V.; Vedyagin, A.A. Synthesis of Ni-Cu-CNF Composite Materials via Carbon Erosion of Ni-Cu Bulk Alloys Prepared by Mechanochemical Alloying. *J. Compos. Sci.* **2023**, *7*, 238. [[CrossRef](#)]
4. Kashimat, N.; Sharma, S.; Nayak, R.; Manjunathaiah, K.B.; Shettar, M.; Chennegowda, G.M. Experimental Investigation of Mechanical Property and Wear Behaviour of T6 Treated A356 Alloy with Minor Addition of Copper and Zinc. *J. Compos. Sci.* **2023**, *7*, 149. [[CrossRef](#)]
5. Rezayat, M.; Yazdi, M.; Noghani, M.; Ahmadi, R. Bactericidal Properties of Copper-Tin Nanoparticles on Escherichia Coli in a Liquid Environment. *Plasma* **2020**, *3*, 153–165. [[CrossRef](#)]
6. Kim, W.; Kim, C.; Lee, W.; Park, J.; Kim, D. Innocuous, Highly Conductive, and Affordable Thermal Interface Material with Copper-Based Multi-Dimensional Filler Design. *Biomolecules* **2021**, *11*, 132. [[CrossRef](#)]
7. Shao, Z.; Jiang, X.; Shu, R.; Wu, Z.; Huang, Z.; Deng, H.; Qin, Q.; Zhu, M. Effect of Cr Micro-Alloying on Microstructure and Mechanical Properties of Alumina Whisker and Graphene Co-Reinforced Copper Matrix Composites. *J. Alloys Compd.* **2022**, *909*, 164804. [[CrossRef](#)]
8. Ashkani, O.; Tavighi, M.R.; Karamimoghadam, M.; Moradi, M.; Bodaghi, M.; Rezayat, M. Influence of Aluminum and Copper on Mechanical Properties of Biocompatible Ti-Mo Alloys: A Simulation-Based Investigation. *Micromachines* **2023**, *14*, 1081. [[CrossRef](#)] [[PubMed](#)]
9. Saghafi Yazdi, M.; Rezayat, M.; Rovira, J.J.R. ElectroCatalytic Activity of Nickel Foam with Co, Mo, and Ni Phosphide Nanostructures. *Plasma* **2022**, *5*, 221–232. [[CrossRef](#)]
10. Abzhlov, R.; Sataev, M.; Koshkarbayeva, S.; Sagitova, G.; Smailov, B.; Azimov, A.; Serikbaeva, B.; Kolesnikova, O.; Fediuk, R.; Amran, M. Studies of the Application of Electrically Conductive Composite Copper Films to Cotton Fabrics. *J. Compos. Sci.* **2022**, *6*, 349. [[CrossRef](#)]
11. Rezayat, M.; Yazdi, M.S.; Zandi, M.D.; Azami, A. Tribological and Corrosion Performance of Electrodeposited Ni-Fe/Al<sub>2</sub>O<sub>3</sub> Coating. *Results Surf. Interfaces* **2022**, *9*, 100083. [[CrossRef](#)]
12. Hwang, S.J.; Lee, J. Mechanochemical Synthesis of Cu–Al<sub>2</sub>O<sub>3</sub> Nanocomposites. *Mater. Sci. Eng. A* **2005**, *405*, 140–146. [[CrossRef](#)]
13. Shehata, F.; Fathy, A.; Abdelhameed, M.; Moustafa, S.F. Fabrication of Copper–Alumina Nanocomposites by Mechano-Chemical Routes. *J. Alloys Compd.* **2009**, *476*, 300–305. [[CrossRef](#)]
14. Korać, M.; Kamberović, Ž.; Anđić, Z.; Stopić, S. Advances in Thermochemical Synthesis and Characterization of the Prepared Copper/Alumina Nanocomposites. *Metals* **2020**, *10*, 719. [[CrossRef](#)]
15. Ponraj, N.V.; Vettivel, S.C.; Azhagurajan, A.; Sahaya Shajan, X.; Nabhiraj, P.Y.; Theivasanthi, T.; Selvakumar, P.; Lenin, A.H. Effect of Milling on Dispersion of Graphene Nanosheet Reinforcement in Different Morphology Copper Powder Matrix. *Surf. Interfaces* **2017**, *9*, 260–265. [[CrossRef](#)]
16. Yue, H.; Yao, L.; Gao, X.; Zhang, S.; Guo, E.; Zhang, H.; Lin, X.; Wang, B. Effect of Ball-Milling and Graphene Contents on the Mechanical Properties and Fracture Mechanisms of Graphene Nanosheets Reinforced Copper Matrix Composites. *J. Alloys Compd.* **2017**, *691*, 755–762. [[CrossRef](#)]
17. Almotairy, S.M.; Alharthi, N.H.; Alharbi, H.F.; Abdo, H.S. Superior Mechanical Performance of Inductively Sintered Al/SiC Nanocomposites Processed by Novel Milling Route. *Sci. Rep.* **2020**, *10*, 10368. [[CrossRef](#)]
18. Rane, A.V.; Kanny, K.; Abitha, V.K.; Thomas, S. Methods for Synthesis of Nanoparticles and Fabrication of Nanocomposites. In *Synthesis of Inorganic Nanomaterials*; Woodhead Publishing: Cambridge, UK, 2018; pp. 121–139. [[CrossRef](#)]
19. Selvaraj, S.K.; Srinivasan, K.; Deshmukh, J.; Agrawal, D.; Mungilwar, S.; Jagtap, R.; Hu, Y.-C. Performance Comparison of Advanced Ceramic Cladding Approaches via Solid-State and Traditional Welding Processes: A Review. *Materials* **2020**, *13*, 5805. [[CrossRef](#)]
20. Kumar, K.S.; Van Swygenhoven, H.; Suresh, S. Mechanical Behavior of Nanocrystalline Metals and Alloys. *Acta Mater.* **2003**, *51*, 5743–5774. [[CrossRef](#)]
21. Chaudhari, A.K.; Singh, V.B. A Review of Fundamental Aspects, Characterization and Applications of Electrodeposited Nanocrystalline Iron Group Metals, Ni-Fe Alloy and Oxide Ceramics Reinforced Nanocomposite Coatings. *J. Alloys Compd.* **2018**, *751*, 194–214. [[CrossRef](#)]
22. Karmakar, R.; Maji, P.; Ghosh, S.K. A Review on the Nickel Based Metal Matrix Composite Coating. *Met. Mater. Int.* **2020**, *27*, 2134–2145. [[CrossRef](#)]
23. Khatua, A.; Kumari, K.; Khatak, D.; Roy, A.; Bhatt, N.; Paul, B.; Naik, A.; Patel, A.K.; Panigrahi, U.K.; Sahu, S.K.; et al. Synthesis and Spectral Characterisation of Fabricated Cerium-Doped Magnesium Oxide Nanoparticles: Evaluation of the Antimicrobial Potential and Its Membranolytic Activity through Large Unilamellar Vesicles. *J. Funct. Biomater.* **2023**, *14*, 112. [[CrossRef](#)] [[PubMed](#)]
24. Alqahtani, K.N.; Nasr, M.M.; Ahmad, S.; Al-Samhan, A.M.; Alhaag, M.H.; Kaid, H. Integrated Intelligent Method Based on Fuzzy Logic for Optimizing Laser Microfabrication Processing of GnP<sub>s</sub>-Improved Alumina Nanocomposites. *Micromachines* **2023**, *14*, 750. [[CrossRef](#)] [[PubMed](#)]
25. Dash, K.; Ray, B.C.; Chaira, D. Synthesis and Characterization of Copper–Alumina Metal Matrix Composite by Conventional and Spark Plasma Sintering. *J. Alloys Compd.* **2012**, *516*, 78–84. [[CrossRef](#)]
26. Wei, K.X.; Zhou, H.R.; Jia, F.L.; Zhang, K.; Wei, W.; Chu, F.Q.; Dan Wang, D.; Alexandrov, I.V. Mechanical Behaviors of Graphene/Copper Matrix Composite Foils Fabricated by Pulse Electrodeposition. *Surf. Interfaces* **2021**, *24*, 101142. [[CrossRef](#)]

27. Venugopal, T.; Rao, K.P.; Murty, B.S. Synthesis of Copper–Alumina Nanocomposite by Reactive Milling. *Mater. Sci. Eng. A* **2005**, *393*, 382–386. [[CrossRef](#)]
28. Khan, I.; Saeed, K.; Khan, I. Nanoparticles: Properties, Applications and Toxicities. *Arab. J. Chem.* **2017**, *12*, 908–931. [[CrossRef](#)]
29. Coetzee, D.; Venkataraman, M.; Militky, J.; Petru, M. Influence of Nanoparticles on Thermal and Electrical Conductivity of Composites. *Polymers* **2020**, *12*, 742. [[CrossRef](#)]
30. Khan, Y.; Sadia, H.; Ali Shah, S.Z.; Khan, M.N.; Shah, A.A.; Ullah, N.; Ullah, M.F.; Bibi, H.; Bafakeeh, O.T.; Khedher, N.B.; et al. Classification, Synthetic, and Characterization Approaches to Nanoparticles, and Their Applications in Various Fields of Nanotechnology: A Review. *Catalysts* **2022**, *12*, 1386. [[CrossRef](#)]
31. Joudeh, N.; Linke, D. Nanoparticle Classification, Physicochemical Properties, Characterization, and Applications: A Comprehensive Review for Biologists. *J. Nanobiotechnol.* **2022**, *20*, 262. [[CrossRef](#)]
32. Cuevas, A.; Vega, V.; Domínguez, A.; González, A.S.; Prida, V.M.; Benavente, J. Optical Characterization of ALD-Coated Nanoporous Alumina Structures: Effect of Sample Geometry or Coated Layer Material. *Micromachines* **2023**, *14*, 839. [[CrossRef](#)]
33. Nagarl, M. Effect of Al<sub>2</sub>O<sub>3</sub> Particles on Mechanical and Wear Properties of 6061al Alloy Metal Matrix Composites. *J. Mater. Sci. Eng.* **2013**, *2*, 1000120. [[CrossRef](#)]
34. Kaya, A.I. Influence of Varying Amounts of Alumina (Al<sub>2</sub>O<sub>3</sub>) on the Wear Behavior of ZnO, SiO<sub>2</sub> and TiO<sub>2</sub> Compounds. *Processes* **2023**, *11*, 1073. [[CrossRef](#)]
35. Khuri, A.I.; Mukhopadhyay, S. Response Surface Methodology. *Wiley Interdiscip. Rev. Comput. Stat.* **2010**, *2*, 128–149. [[CrossRef](#)]
36. Chelladurai, S.J.S.; Murugan, K.; Ray, A.P.; Upadhyaya, M.; Narasimharaj, V.; Gnanasekaran, S. Optimization of Process Parameters Using Response Surface Methodology: A Review. *Mater. Today Proc.* **2021**, *37*, 1301–1304. [[CrossRef](#)]
37. Rajeshkumar, L.N.; Amirthagadeswaran, K.S. Variations in the Properties of Copper–Alumina Nanocomposites Synthesized by Mechanical Alloying. *Mater. Technol.* **2019**, *53*, 57–63. [[CrossRef](#)]
38. Mohammed, M.M.M.; Elkady, O.A.; Abdelhameed, A.W. Effect of Alumina Particles Addition on Physico-Mechanical Properties of AL-Matrix Composites. *Open J. Met.* **2013**, *3*, 72–79. [[CrossRef](#)]
39. Salahi, E.; Rajabi, A. Fabrication and Characterisation of Copper–Alumina Nanocomposites Prepared by High-Energy Fast Milling. *Mater. Sci. Technol.* **2016**, *32*, 1212–1217. [[CrossRef](#)]
40. Zawrah, M.F.; Abdel-kader, H.; Elbaly, N.E. Fabrication of Al<sub>2</sub>O<sub>3</sub>–20vol.% Al Nanocomposite Powders Using High Energy Milling and Their Sinterability. *Mater. Res. Bull.* **2012**, *47*, 655–661. [[CrossRef](#)]
41. Ying, D.Y.; Zhang, D.L. Solid-State Reactions between Cu and Al during Mechanical Alloying and Heat Treatment. *J. Alloys Compd.* **2000**, *311*, 275–282. [[CrossRef](#)]
42. Fogagnolo, J.B.; Amador, D.; Ruiz-Navas, E.M.; Torralba, J.M. Solid Solution in Al–4.5wt% Cu Produced by Mechanical Alloying. *Mater. Sci. Eng. A* **2006**, *433*, 45–49. [[CrossRef](#)]
43. An, L.-Y.; Dai, Z.; Di, B.; Xu, L.-L. Advances in Cryochemistry: Mechanisms, Reactions and Applications. *Molecules* **2021**, *26*, 750. [[CrossRef](#)] [[PubMed](#)]

**Disclaimer/Publisher’s Note:** The statements, opinions and data contained in all publications are solely those of the individual author(s) and contributor(s) and not of MDPI and/or the editor(s). MDPI and/or the editor(s) disclaim responsibility for any injury to people or property resulting from any ideas, methods, instructions or products referred to in the content.